Article

Long-range ordered porous carbons produced from C_{60}

Fei Pan[1,15], Kun Ni[1,15], Tao Xu[2,15], Huaican Chen[3,4], Yusong Wang[5], Ke Gong[5], Cai Liu[6,7,8], Xin Li[5], Miao-Ling Lin[9], Shengyuan Li[1], Xia Wang[1], Wensheng Yan[10], Wen Yin[3,4], Ping-Heng Tan[9], Litao Sun[2], Dapeng Yu[6,7,8], Rodney S. Ruoff[11,12,13,14 ✉] & Yanwu Zhu[1,5 ✉]

Carbon structures with covalent bonds connecting C_{60} molecules have been reported[1-3], but their production methods typically result in very small amounts of sample, which restrict the detailed characterization and exploration necessary for potential applications. We report the gram-scale preparation of a new type of carbon, long-range ordered porous carbon (LOPC), from C_{60} powder catalysed by α-Li_3N at ambient pressure. LOPC consists of connected broken C_{60} cages that maintain long-range periodicity, and has been characterized by X-ray diffraction, Raman spectroscopy, magic-angle spinning solid-state nuclear magnetic resonance spectroscopy, aberration-corrected transmission electron microscopy and neutron scattering. Numerical simulations based on a neural network show that LOPC is a metastable structure produced during the transformation from fullerene-type to graphene-type carbons. At a lower temperature, shorter annealing time or by using less α-Li_3N, a well-known polymerized C_{60} crystal forms owing to the electron transfer from α-Li_3N to C_{60}. The carbon K-edge near-edge X-ray absorption fine structure shows a higher degree of delocalization of electrons in LOPC than in C_{60}(s). The electrical conductivity is 1.17×10^{-2} S cm^{-1} at room temperature, and conduction at $T < 30$ K appears to result from a combination of metallic-like transport over short distances punctuated by carrier hopping. The preparation of LOPC enables the discovery of other crystalline carbons starting from C_{60}(s).

C_{60} crystallizes as a face-centred-cubic (fcc) molecular crystal[4,5] with molecular rotation phase transitions sensitive to temperature and pressure[6,7]. 'Fullerene polymers' are obtained by treating C_{60}(s) at high pressure and high temperature (HPHT)[8,9], by high-speed vibration milling[10], by doping C_{60}(s) with alkali metals[11,12] and by exposing C_{60}(s) to an electron beam[13] or ultraviolet irradiation[14]. A monolayer polymeric C_{60} network was recently prepared by an interlayer bonding cleavage strategy[15]. Long-range ordered carbon clusters, a unique crystalline material made of amorphous building blocks, have been synthesized by crushing C_{60} cages at high pressure and room temperature[16]. Superhard amorphous carbons produced by HPHT processing of C_{60} crystals have also been reported[17-19]. Carbon crystals with extensive covalent bonding could have an exceptional hardness[16], but the reported quantity of carbons made by HPHT treatment is typically very small because of the size of the high-pressure cell they are made in, so that assessing their properties is challenging. A chemical protocol for their large-scale preparation enabling more detailed characterization of the long-range ordered carbons products would clearly be helpful.

Characterization

We found that α-Li_3N catalyses covalent bonding between C_{60} molecules at 550 °C at ambient pressure (as detailed in the Methods), leading to what we refer to as long-range ordered porous carbon (LOPC) crystals. Scanning electron microscope (SEM) images show that LOPC maintains the grain-like morphology of the original C_{60} crystals with some crystal facets. One suggested structure for LOPC is shown in Fig. 1a. Figure 1b shows the X-ray diffraction patterns of (1) C_{60}(s) that is fcc (space group: $Fm\overline{3}m$) and (2) LOPC with broader peaks of the fcc C_{60}(s), but with long-range periodicity remaining. By a modelling study (detailed in the Methods and Supplementary Fig. 1) and Rietveld refinement, which involves searching structures close in energy to the fcc C_{60} crystal, we found LOPC to be a 'long-range ordered metastable

[1]Department of Materials Science and Engineering, School of Chemistry and Materials Science, University of Science and Technology of China, Hefei, China. [2]SEU-FEI Nano-Pico Center and Key Laboratory of MEMS of Ministry of Education, Southeast University, Nanjing, China. [3]Institute of High Energy Physics, Chinese Academy of Sciences, Beijing, China. [4]Spallation Neutron Source Science Center, Dongguan, China. [5]Hefei National Research Center for Physical Sciences at the Microscale, University of Science and Technology of China, Hefei, China. [6]International Quantum Academy, Shenzhen, China. [7]Shenzhen Institute for Quantum Science and Engineering, Southern University of Science and Technology, Shenzhen, China. [8]Guangdong Provincial Key Laboratory of Quantum Science and Engineering, Southern University of Science and Technology, Shenzhen, China. [9]State Key Laboratory of Superlattices and Microstructures, Institute of Semiconductors, Chinese Academy of Sciences, Beijing, China. [10]National Synchrotron Radiation Laboratory, University of Science and Technology of China, Hefei, China. [11]Center for Multidimensional Carbon Materials, Institute for Basic Science, Ulsan, Republic of Korea. [12]Department of Chemistry, Ulsan National Institute of Science and Technology (UNIST), Ulsan, Republic of Korea. [13]Department of Materials Science and Engineering, UNIST, Ulsan, Republic of Korea. [14]School of Energy and Chemical Engineering, UNIST, Ulsan, Republic of Korea. [15]These authors contributed equally: Fei Pan, Kun Ni, Tao Xu. ✉e-mail: rsuoff@ibs.re.kr; zhuyanwu@ustc.edu.cn
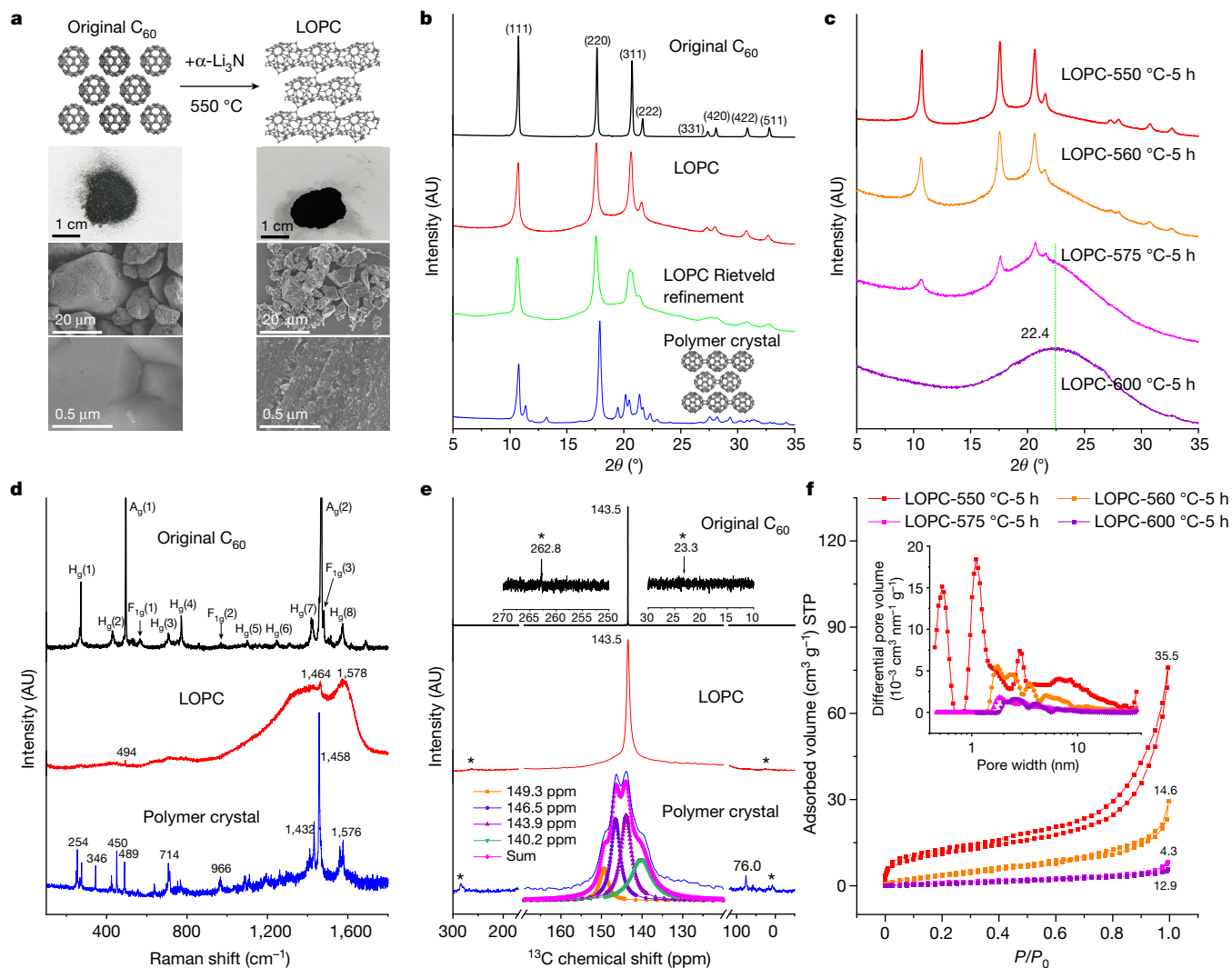
Fig. 1 | Morphological and structural characterizations. a, Atomic structure models, optical and SEM images. **b**, Cu Kα (λ = 0.15418 nm) X-ray diffraction patterns with simulation for LOPC, based on the proposed atomic structure model. AU, arbitrary units. **c**, X-ray diffraction patterns of LOPCs, with the temperature the samples were prepared at indicated. **d**, Raman spectra for the original C_{60}, LOPC and the polymer crystal. **e**, ^{13}C MAS-SSNMR spectra. The pink line shows the Lorentz fit of peaks for the polymer crystal; '*' indicates the spinning side bands. **f**, Low-pressure Ar (87.3 K) adsorption/desorption isotherms and (inset) pore-size distribution (calculated by using a slit pore with a DFT equilibrium model) for LOPCs, with specific surface area values ($m^2 g^{-1}$) labelled above each of the isotherm curves.

phase' between fcc C_{60} and graphite. When the annealing temperature was reduced to 480 °C while keeping all other conditions unchanged, a C_{60} polymer crystal was obtained, with an orthorhombic structure (space group: *Pmnn*), composed of one-dimensional (1D) C_{60} polymer chains[20]. Characterization (Fig. 1b and Supplementary Fig. 2) shows that the polymer crystal consists of C_{60} cages connected along the <110> direction with two sp^3 bonds formed between facing hexagons[21]; the micrometre-sized crystals demonstrate the advantage of the current preparation strategy, because most C_{60} polymers previously obtained are oligomers consisting of several connected cages[14,22]. When the annealing temperature is above 550 °C, X-ray diffraction patterns (Fig. 1c) of LOPCs show diminishing peaks and a gradually rising background, which eventually becomes a hump centred at 2θ = 22.4° for the carbon prepared at 600 °C. A broader parametric study of the preparation indicates that the formation of LOPC occurs in a narrow range of combined conditions of α-Li_3N/C_{60} ratio, annealing temperature and time (Supplementary Fig. 3).

A typical Raman spectrum (Fig. 1d) of LOPC features two broad bands with a sharp peak at 1,464 cm^{-1} (more spectra in Supplementary Fig. 4). Such a peak is attributed to a pentagon stretching mode in the

proposed structure (1,449 cm^{-1} in Supplementary Fig. 5 and Supplementary Video 1), also close to the $A_g(2)$ peak of C_{60} (Supplementary Video 2) and the peak at 1,473 cm^{-1} of a C_{60} polymer crystal (Supplementary Videos 3 and 4), which becomes smeared for carbons made at higher temperatures (Supplementary Fig. 6). The broad contour of the Raman spectrum may be contributed by multiple LOPCs with slightly different atomic structures (Supplementary Fig. 7). Compared to the spectrum of C_{60}, the extra Raman peak at 966 cm^{-1} in the experimental pattern, or at 954 cm^{-1} in the simulated pattern, for the C_{60} polymer crystal is attributed to a 'tetragonal pinch', a stretching vibration of sp^3 carbon bonding between cages (Supplementary Figs. 8 and 9 and Supplementary Table 1)[20].

Figure 1e shows the magic-angle-spinning solid-state NMR (MAS-SSNMR) spectra. The sharp resonance at 143.5 ppm corresponds to C_{60} in rapid rotation[23]. The broadening of the NMR peak for LOPC indicates a more complicated environment of the carbon atoms[24]. The peak at 76.0 ppm in the NMR spectrum of the polymer crystal has been previously attributed to sp^3 bonding between C_{60} molecules[10,25]. The ratio of sp^3 bonding to all C atom ($sp^2 + sp^3$) bonding is estimated as approximately 0.053, reasonably close to the simulated value of
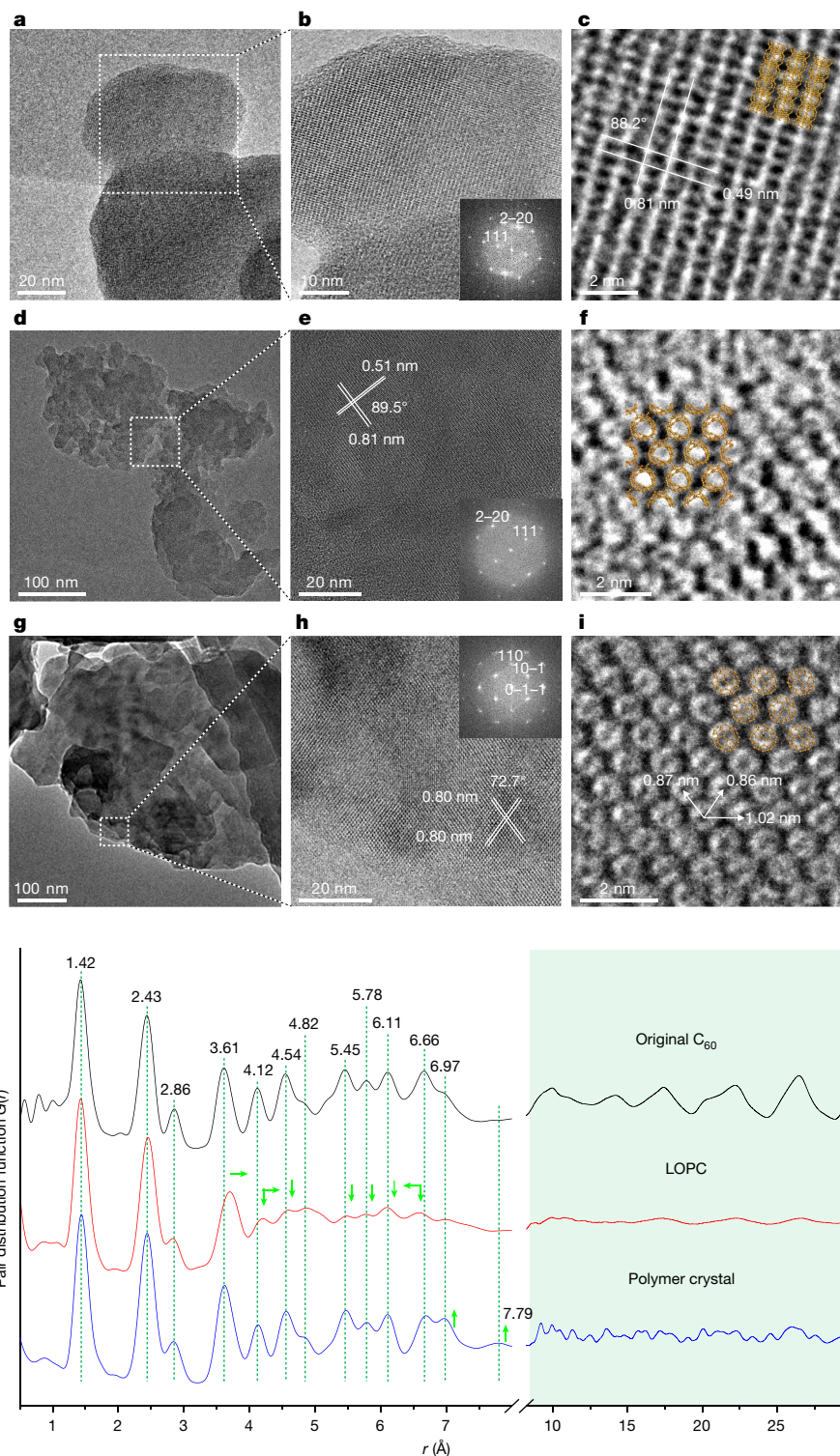
Fig. 2 | Microstructure characterization. a, TEM image of the original C_{60} particles. **b**, Enlarged view with a FFT in the inset. **c**, High-resolution image showing the spacings of the (111) (0.81 nm) and (220) planes (0.49 nm) of fcc C_{60}. **d**, Typical TEM image of LOPC particles. **e**, Enlarged view and FFT (inset). **f**, High-resolution image showing deformed and connected cages in the LOPC crystal. **g**, Typical TEM image of polymer crystal particles. **h**, Enlarged view and FFT (inset). **i**, High-resolution image showing individual C_{60} cages with centre-to-centre distances labelled in the polymer crystal; the suggested structure is shown by the orange-coloured overlayers in **c**, **f** and **i** for each carbon. **j**, Neutron PDF for the original C_{60}, LOPC and the polymer crystal. Distances are labelled for the major peaks below 0.7 nm, which is the diameter of a C_{60} cage. Green arrows indicate the changes of peak positions and intensities in LOPC and polymer crystal, compared to the original C_{60}.

0.067 based on the calculated NMR spectrum (Supplementary Fig. 10 and Supplementary Table 2) and the value of 0.052 reported for the orthorhombic structure made by HPHT[25].

From the Ar adsorption/desorption isotherms and pore-size distributions (Fig. 1f) we can see that LOPC is porous, with a Brunauer–Emmett–Teller specific surface area of 4.3 to 35.5 $m^2 g^{-1}$ in the range of the
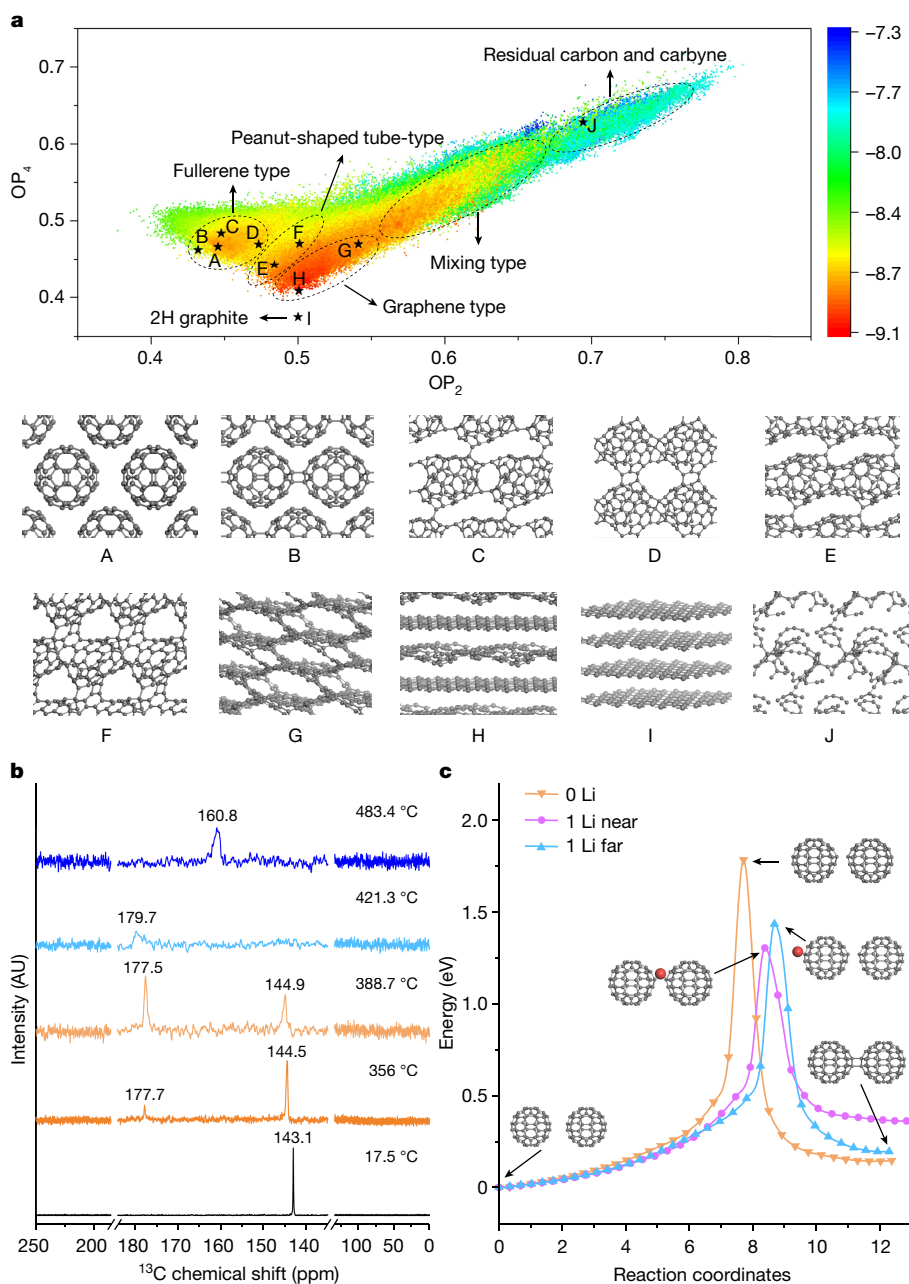
Fig. 3 | Simulations and in situ MAS-SSNMR. a, Potential energy surface nearby fcc C_{60} expressed with Steinhardt-type order parameter (OP). According to the geometric characteristics of the carbons obtained, five distinct regions are circled to guide the eye, and the representative structures are listed for four of these: (A) fcc C_{60}, (B) polymer crystal composed of 1D fullerene polymer chains, (C) polymer crystal composed of 2D fullerene polymer network, (D) polymer crystal composed of 2D fullerene polymer network with rings as connection, (E) 1D peanut-shaped tube with intertube polymerization,
(F) open-caged peanut-shaped tube, (G) 3D connected graphene-like structure, (H) 2D curved graphene-like structure, (I) 2H graphite, and (J) residual carbyne. **b**, ^{13}C chemical shift spectra depending on temperature, obtained from in situ MAS-SSNMR data while heating 500 mg C_{60} with 100 mg α-Li_3N. **c**, Calculated reaction energy path of 2+2 polymerization of two isolated C_{60} cages without Li adsorption ('0 Li'), with one Li atom adsorbed near the sp^3 bonding site ('1 Li near') or one Li atom adsorbed far from the sp^3 bonding ('1 Li far').

preparation parameters shown. Electron spin resonance measurements (Supplementary Fig. 11) show that it has a higher number of unpaired spins than the original C_{60} and the polymer crystal. Elemental analysis using X-ray photoelectron spectroscopy (Supplementary Fig. 12) shows that the carbon concentration for the original C_{60} is 98 at.% with 1.3 at.% oxygen, and for LOPC it is 89 at.% carbon with 8.6 at.% oxygen. The at.% of nitrogen or lithium (Li) is less than 1 at.%, and a very low content of Li has been verified by thermogravimetric analysis (Supplementary

Fig. 13). The differential scanning calorimetry curves in Supplementary Fig. 14 indicate that the orientation-ordering transition observed in fcc C_{60} (ref. [26]) is not present in LOPC or in the polymer crystal. However, when the polymer crystal was heated to 400 °C followed by cooling, the transition reappeared, suggesting that the polymer crystal decomposed to C_{60} molecules after heating[9]. By contrast, LOPC remained stable at temperatures up to about 500 °C and heating it at higher temperatures led to a deterioration of the long-range order (Supplementary
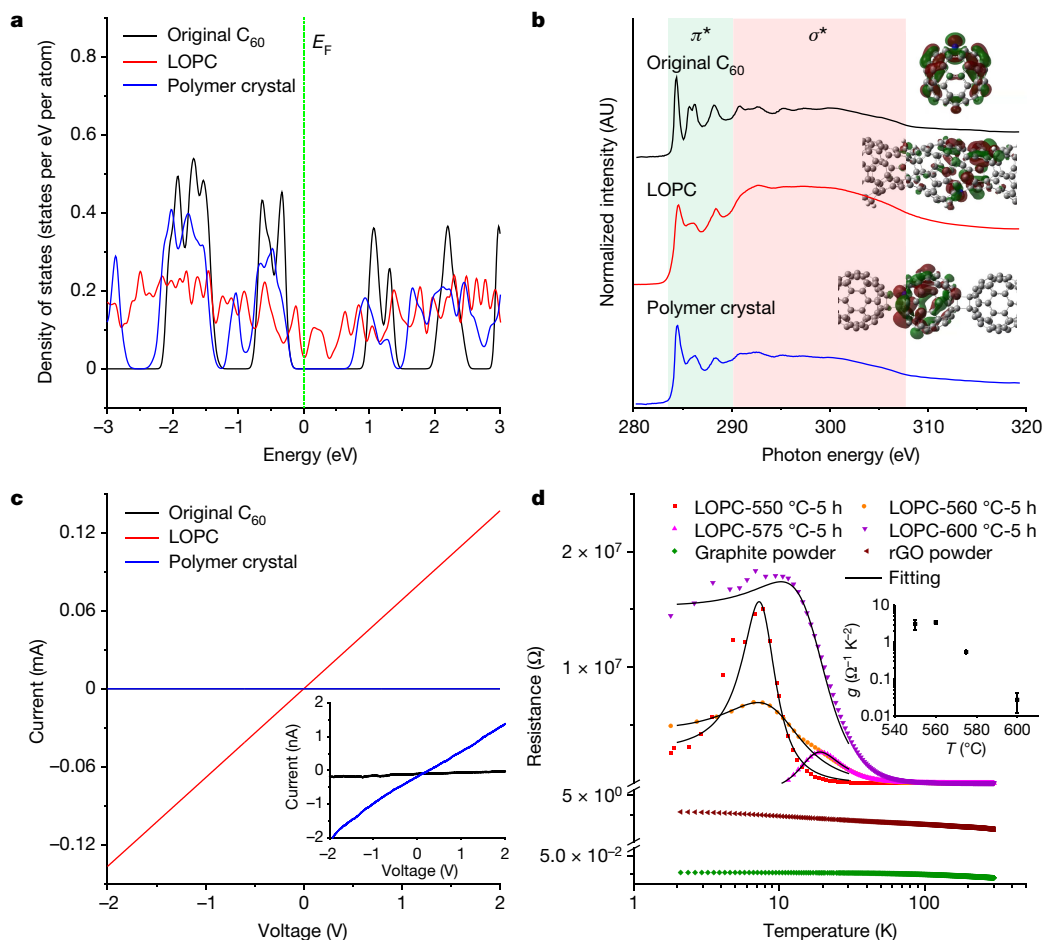
Fig. 4 | DOS, NEXAFS and electrical conductivity measurements. a, Density of states. **b**, Carbon K-edge NEXAFS spectra. Insets show the simulated final-state molecular orbitals of the excited atoms for the first prominent peak (284.4 eV for the original C_{60}, 285.0 eV for LOPC or 284.2 eV for the polymer crystal). Atoms marked blue are excited atoms (isovalue = 0.02). **c**, Direct current voltage–current curves of three membranes made by mixing each carbon with 5 wt% polytetrafluoroethylene. Inset shows an enlarged view of the ordinate. Electrical conductivities calculated from the curves are

2.44×10^{-9} S cm^{-1}, 7.39×10^{-8} S cm^{-1} and 1.17×10^{-2} S cm^{-1} for the original C_{60}, polymer crystal and LOPC, respectively. **d**, Resistivity testing for the LOPCs, graphite powder and rGO powder. The curves for the LOPCs are fitted by formula: $\rho = \dfrac{a}{\frac{b}{c + T^2} + d + gT^2}$, where a, b, c and d are fitting parameters, and g is a constant dependent on the barrier geometry[38]. The inset shows the change of g value with the annealing temperature of the LOPC.

Fig. 15). The relative amount of residual C_{60} in LOPC and the polymer crystal is estimated as approximately 3% from a comparison of the mass spectra (Supplementary Fig. 16).

The fcc structure of the original C_{60}(s) was identified by transmission electron microscopy (TEM) as shown in Fig. 2a,b and the corresponding fast Fourier transform (FFT). The labelled spacings in Fig. 2c are attributed to the (111) and (220) planes in fcc C_{60}. Individual cages could not be observed with atomic resolution because of the rapid rotation of the C_{60} molecules at room temperature[6,23]. Figure 2d shows that LOPC has long-range order, with lattice fringes observed in the enlarged image in Fig. 2e. The FFT of Fig. 2e is close to that of the original C_{60}, but there is a distortion. Although the detailed atomic-scale connection between cages in LOPC could not be observed, individual cages were distinguished, with structural parameters consistent with the suggested model (Fig. 2f). The images in Fig. 2g,h confirm the orthorhombic structure, which is composed of linear C_{60} polymer chains, with a measured spacing of 0.80 nm, corresponding to the (011) or (101) interplanar spacings[27]. Because covalent bonds are formed between the cages, individual C_{60} molecules are distinguished in the TEM image in Fig. 2i. More TEM images are shown in Supplementary Fig. 17.

The atomic structure of LOPC was investigated using the neutron diffraction pair distribution function (PDF)[28], by comparing it to a C_{60}

molecular crystal and a C_{60} polymer crystal. As shown in Fig. 2j, no obvious changes were observed for bonds with lengths smaller than 3 Å, indicating that trivalent carbon bonding remains dominant in the new carbon. In the long-distance range (>9 Å), LOPC had vanishing peaks because of the great disorder, but more peaks were identified for the C_{60} polymer crystal because of the suppressed rotation of the C_{60} cages, consistent with more 'fine structure' observed in the Raman (Fig. 1d) and Fourier transform infrared (FTIR) spectra (Supplementary Fig. 18). In the 3–8 Å range, the larger bond lengths at 3.6 and 4.1 Å observed in the PDF of LOPC may be explained by the reduced curvature in broken C_{60} cages, when we compare them with the similar lengths in graphite (Supplementary Fig. 19). The strong peak at 7 Å and hump at 7.8 Å observed in the polymer crystal correspond to distances in the deformed cages along the bonding direction (Supplementary Fig. 20).

Simulations and mechanism

An extensive search of the potential energy surface (PES) in regions near fcc C_{60} at ambient pressure was performed to understand the formation of the LOPC crystal[29]. Using the neural network of carbon (detailed in the Methods), a total of 346,516 structures were sampled[30]. The two-dimensional representation of the PES is shown in Fig. 3a,

Article

from which we could identify four regions corresponding to distinct carbon structures: that is, residual carbon and carbyne, fullerene-type, peanut-shaped tube-type and graphene-type, which are illustrated in Supplementary Fig. 21. Typical structures are shown by structures A to J in the insets, and more structures can be found in Supplementary Fig. 1 and the appendix of the Supplementary Information. Energy mapping suggests a geometrical evolution from fullerene-type to graphene-type structures via peanut-shaped tube-type metaphases; a polymer crystal (structure B) and LOPC (represented by structure E) crystals are among many possible metastable structures in such a route.

Understanding the formation mechanism of C_{60} polymer crystals could provide insight as to the role of α-Li$_3$N. Compared to conditions without α-Li$_3$N, in situ MAS-SSNMR conducted on C_{60} powder with α-Li$_3$N (Fig. 3b and Supplementary Fig. 22) shows a downshift with a broadening of the ^{13}C chemical shift peak and a splitting of the peak at about 145 ppm observed at 388.7 °C, owing to a breaking of symmetry. The appearance of two new peaks at approximately 178 ppm at temperatures above 356 °C and at approximately 159 ppm at temperatures above 453 °C has been attributed to $C_{60}^{(3-)}$ ions[31] and $C_{60}^{(6-)}$ ions[32] in previous studies.

Inspired by the charge injection from α-Li$_3$N to graphite[33], our density functional theory (DFT) simulation shows that the adsorption of Li also introduces a dipole on C_{60} owing to charge transfer, which sequentially induces another dipole on a C_{60} molecule nearby (Supplementary Fig. 23). Figure 3c shows that the energy barrier for the formation of bonds between two isolated C_{60} cages is reduced by the introduced Li atom. The presence of Li has been supported by ab initio molecular dynamics (AIMD) simulations (Supplementary Fig. 24) and X-ray diffraction data of the C_{60} polymer crystal samples before washing (Supplementary Fig. 25), connecting this study to previous ones dealing with Li-doped C_{60}(s)[34,35]. More Li and/or annealing at higher temperatures may break the C_{60} cages and connect the broken species (Supplementary Fig. 26), which inevitably induces defects, as supported by the ^{7}Li MAS NMR spectra (Supplementary Fig. 27)[36].

Measurement of properties

The density of states (DOS) shown in Fig. 4a suggests a very narrow band gap or a conducting nature of LOPC on the basis of the proposed structure in Fig. 1a. The difference in DOS compared to the fcc C_{60} crystal explains the absence of an absorption edge measured by UV–visible spectroscopy (Supplementary Fig. 28) and the diminishing photoluminescence (PL) peak in LOPC (Supplementary Fig. 29). The carbon K-edge near-edge X-ray adsorption fine structure (NEXAFS) spectra in Fig. 4b show that the π* peaks are weaker and broader in the LOPC crystal than in the fcc C_{60} and polymer crystals, indicating complex energy transitions of C 1s → π* in LOPC rather than the well-defined transitions in C_{60}(s)[37]. The insets in Fig. 4b show the orbital distribution of the excited atoms (marked as blue), indicating a significant contribution from the neck region of the LOPC, whereas the C_{60} polymer crystal mainly involves orbitals on the cage with only a very small contribution from the sp^3 bonding between cages. More simulations of carbon K- edge NEXAFS spectra are shown in Supplementary Fig. 30.

The above electronic structure studies indicate greater delocalization of the electrons in LOPC. This is a good match to the electrical measurements, in which LOPC shows the highest electrical conductivity as calculated from the curves in Fig. 4c. When the measurement is performed at 2 K, the resistivity of LOPC is dramatically different from that of graphite or reduced graphite oxide (rGO) powders. As shown in Fig. 4d, all LOPCs, although prepared at different temperatures, feature a sudden increase of resistivity at 10–20 K by 4–5 orders of magnitude and then a drop at the lower temperatures. A hybrid model considering conducting and tunnelling (or hopping) transport of electrons was used to fit the LOPC curves to obtain a parameter g, which depends on the barrier geometry of the semiconducting component[38]. As shown in the inset of Fig. 4d, the g value gradually decreases from 3.12 ± 0.96 to 0.027 ± 0.015 $\Omega^{-1} K^{-2}$ when the annealing temperature increases from 550 to 600 °C, indicating a transition from semiconducting-like to metallic-like properties.

In conclusion, mixing α-Li$_3$N and C_{60}(s) at room pressure and moderate temperatures yields a long-range ordered porous carbon, LOPC, consisting of broken C_{60} cages mainly connected by sp^2 carbon bonding. The LOPC has been extensively characterized experimentally by comparing it with the original fcc C_{60} and another allotrope, a C_{60} polymer crystal. Through simulation we have shown that LOPC is a metastable structure that occurs in the transition from fullerene-type to graphene-type carbons, showing a property transition from semiconducting-like to metallic-like with increasing annealing temperature. Our synthesis was readily performed at the half gram scale, which yielded enough material for the characterization methods we have described. We do not see any reason why this synthesis could not be done at, say, the kilogram scale or larger. Larger quantities would create opportunities to use the products in new ways, and enable further chemistry to generate other downstream products with interesting properties and other functionalities.

Online content

Any methods, additional references, Nature Portfolio reporting summaries, source data, extended data, supplementary information, acknowledgements, peer review information; details of author contributions and competing interests; and statements of data and code availability are available at https://doi.org/10.1038/s41586-022-05532-0.

1. O'Keeffe, M. C_{60} zeolites? Nature **352**, 674–674 (1991).
2. Vanderbilt, D. & Tersoff, J. Negative-curvature fullerene analog of C_{60}. Phys. Rev. Lett. **68**, 511–513 (1992).
3. Okada, S., Saito, S. & Oshiyama, A. New metallic crystalline carbon: three dimensionally polymerized C_{60} fullerite. Phys. Rev. Lett. **83**, 1986–1989 (1999).
4. Krätschmer, W., Lamb, L. D., Fostiropoulos, K. & Huffman, D. R. Solid C_{60}: a new form of carbon. Nature **347**, 354–358 (1990).
5. Quo, Y., Karasawa, N. & Goddard, W. A. Prediction of fullerene packing in C_{60} and C_{70} crystals. Nature **351**, 464–467 (1991).
6. Heiney, P. A. et al. Orientational ordering transition in solid C_{60}. Phys. Rev. Lett. **66**, 2911–2914 (1991).
7. Samara, G. et al. Pressure dependence of the orientational ordering in solid C_{60}. Phys. Rev. Lett. **67**, 3136–3139 (1991).
8. Iwasa, Y. et al. New phases of C_{60} synthesized at high pressure. Science **264**, 1570–1572 (1994).
9. Nunez-Regueiro, M., Marques, L., Hodeau, J.-L., Béthoux, O. & Perroux, M. Polymerized fullerite structures. Phys. Rev. Lett. **74**, 278–281 (1995).
10. Wang, G., Komatsu, K., Murata, Y. & Shiro, M. Synthesis and X-ray structure of dumb-bell-shaped C_{120}. Nature **387**, 583–586 (1997).
11. Margadonna, S. et al. Li$_4$C$_{60}$: a polymeric fulleride with a two-dimensional architecture and mixed interfullerene bonding motifs. J. Am. Chem. Soc. **126**, 15032–15033 (2004).
12. Stephens, P. W. et al. Polymeric fullerene chains in RbC$_{60}$ and KC$_{60}$. Nature **370**, 636–639 (1994).
13. Zhao, Y., Poirier, D., Pechman, R. & Weaver, J. Electron stimulated polymerization of solid C_{60}. Appl. Phys. Lett. **64**, 577–579 (1994).
14. Rao, A. et al. Photoinduced polymerization of solid C_{60} films. Science **259**, 955–957 (1993).
15. Hou, L. et al. Synthesis of a monolayer fullerene network. Nature **606**, 507–510 (2022).
16. Wang, L. et al. Long-range ordered carbon clusters: a crystalline material with amorphous building blocks. Science **337**, 825–828 (2012).
17. Zhang, S. et al. Discovery of carbon-based strongest and hardest amorphous material. Natl Sci. Rev. **9**, nwab140 (2022).
18. Shang, Y. et al. Ultrahard bulk amorphous carbon from collapsed fullerene. Nature **599**, 599–604 (2021).
19. Tang, H. et al. Synthesis of paracrystalline diamond. Nature **599**, 605–610 (2021).
20. Davydov, V. A. et al. Spectroscopic study of pressure-polymerized phases of C_{60}. Phys. Rev. B **61**, 11936–11945 (2000).
21. Okotrub, A. et al. Electronic structure and properties of rhombohedrally polymerized C_{60}. J. Chem. Phys. **115**, 5637–5641 (2001).
22. Burger, B., Winter, J. & Kuzmany, H. Dimer and cluster formation in C_{60} photoreaction. Z. Phys. B **101**, 227–233 (1996).
23. Yannoni, C., Johnson, R., Meijer, G., Bethune, D. & Salem, J. ^{13}C NMR study of the C_{60} cluster in the solid state: molecular motion and carbon chemical shift anisotropy. J. Phys. Chem. **95**, 9–10 (1991).
24. Hiroyama, Y. & Kume, K. High resolution ^{13}C NMR spectra in graphite chemical shift and diamagnetism. Solid State Commun. **65**, 617–619 (1988).
25. Rachdi, F. et al. High resolution NMR studies of one and two dimensional polymerized C_{60}. Appl. Phys. A **64**, 295–299 (1997).

26. Gugenberger, F. et al. Glass transition in single-crystal C_{60} studied by high-resolution dilatometry. *Phys. Rev. Lett.* **69**, 3774–3777 (1992).

27. Sundar, C. et al. Pressure-induced polymerization of fullerenes: a comparative study of C_{60} and C_{70}. *Phys. Rev. B* **53**, 8180–8183 (1996).

28. Juhás, P., Cherba, D., Duxbury, P., Punch, W. & Billinge, S. Ab initio determination of solid-state nanostructure. *Nature* **440**, 655–658 (2006).

29. Ni, K., Pan, F. & Zhu, Y. Structural evolution of C_{60} molecular crystal predicted by neural network potential. *Adv. Funct. Mater.* **32**, 2203894 (2022).

30. Huang, S., Shang, C., Zhang, X. & Liu, Z. Material discovery by combining stochastic surface walking global optimization with a neural network. *Chem. Sci.* **8**, 6327–6337 (2017).

31. Tycko, R. et al. ^{13}C NMR spectroscopy of K_xC_{60}: phase separation, molecular dynamics, and metallic properties. *Science* **253**, 884–886 (1991).

32. Pennington, C. H. & Stenger, V. A. Nuclear magnetic resonance of C_{60} and fulleride superconductors. *Rev. Mod. Phys.* **68**, 855–910 (1996).

33. Pan, F. et al. Phase-changing in graphite assisted by interface charge injection. *Nano Lett.* **21**, 5648–5654 (2021).

34. Wågberg, T., Stenmark, P. & Sundqvist, B. Structural aspects of two-dimensional polymers: Li_4C_{60}, Na_4C_{60} and tetragonal C_{60}. Raman spectroscopy and X-ray diffraction. *J. Phys. Chem. Solids* **65**, 317–320 (2004).

35. Wågberg, T. & Johnels, D. ^7Li and ^{23}Na MAS solid state NMR studies of Na_4C_{60} and Li_4C_{60}. *J. Phys. Chem. Solids* **67**, 1091–1094 (2006).

36. Aoyagi, S. et al. A layered ionic crystal of polar $Li@C_{60}$ superatoms. *Nat. Chem.* **2**, 678–683 (2010).

37. Terminello, L. et al. Unfilled orbitals of C_{60} and C_{70} from carbon K-shell X-ray absorption fine structure. *Chem. Phys. Lett.* **182**, 491–496 (1991).

38. Uher, C., Hockey, R. & Ben-Jacob, E. Pressure dependence of the c-axis resistivity of graphite. *Phys. Rev. B* **35**, 4483–4488 (1987).

Article

Methods

Preparation and purification of LOPCs and C_{60} polymer crystal

In a typical preparation, 500 mg C_{60} powder (Suzhou Dade Carbon Nano Technology, 99.5 at.%) without any grinding was loaded into a 150 mm long, 15 mm diameter quartz tube closed at one end and 100 mg α-Li_3N powder (Sigma-Aldrich, 99.5 wt%, or Alfa Aesar, 99.4 wt%) was added to the same tube in a glovebox with an Ar(g) atmosphere. The two powders were mixed by shaking the tube, which was then sealed at a high temperature in a vacuum. The sealed quartz tube containing the mixed powders was heated from room temperature to 550 °C for LOPC, or 480 °C for the C_{60} polymer crystal, at a heating rate of 5 °C min^{-1} in an Ar atmosphere (flow rate, 100 sccm) in a horizontal tube furnace, followed by holding at 550 °C for LOPC, or 480 °C for the C_{60} polymer crystal, for 5 h. Higher temperatures, for example, 560, 575 and 600 °C, were also tried for the preparation of LOPCs, while keeping the other conditions unchanged.

To remove unreacted C_{60} or residuals, the LOPC and polymer crystal samples were subjected to harsh washing and heating; the detailed procedures are included in the Supplementary Information. Note that X-ray diffraction studies before or during washing (Supplementary Fig. 31) indicate that the C_{60} polymer crystal or LOPC is formed before washing, because the disappearing diffraction peaks after washing with toluene are only ascribed to fcc C_{60} or Li_4C_{60}, and the diffraction peaks of C_{60} polymer crystal or LOPC remain nearly unchanged before and after washing. The peaks ascribed to Li_2CO_3 disappear after subsequent washing with deionized water.

Characterization

To characterize the materials we used SEM (Zeiss GeminiSEM 500, operating at 3 kV), X-ray diffraction (Rigaku SmartLab, Cu Kα), Raman (Jobin-Yvon, 532 nm), FTIR (Thermo Fisher Nicolet 6700, diluted with KBr), thermogravimetric analysis (Netszch TG 209 F1 Libra), differential scanning calorimetry (TA Instruments, DSC Q2000 V24.10 Build 122), MALDI-TOF (Bruker Autoflex Speed TOF/TOF), TEM (FEI Titan 80–300, operating at 80 kV, and FEI Tecnai G20, operating at 200 kV), X-ray photoelectron spectroscopy (Thermo Scientific ESCALAB 250, AlK$_α$), ESR (JEOL JES-FA200), Ar adsorption/desorption (Quantachrome Autosorb iQ$_3$) using Brunauer–Emmett–Teller method and ^{13}C MAS-SSNMR (Brucker Avance III 400 MHz WB) with a 4 mm HX probe operated at 100.61 MHz for measurement at room temperature and a 7 mm laser heated HX probe for in situ measurements. Neutron total scattering measurements were performed on a Multiple Physics Instrument at the China Spallation Neutron Source (CSNS)[39]; in each measurement, 800–1,000 mg of powder was measured for 12 h at ambient conditions. The total neutron scattering data were processed using the Mantid software[40] and Fourier transformation to obtain the pair distribution functions with a maximum momentum transfer $Q_{max} = 30$ Å^{-1}. More parameters used in the characterizations are included in the Supplementary Information.

Measurement of properties

UV–visible adsorption measurements were made with a UV–visible spectrophotometer (Shimadzu Solid 3700), and PL spectra were obtained using a steady-state/lifetime spectrofluorometer (Horiba JY Fluorolog-3-tau). The NEXAFS data were obtained at the (BL12B) beamlines MCD-A and MCD-B (Soochow Beamline for Energy Materials) of the National Synchrotron Radiation Laboratory (Hefei, China) under the total electron yield mode. The room-temperature conductivities of all the powder samples were measured using a semiconductor characterization system (Keithley 4200-SCS) with a two-point probe method. Measurement of temperature dependence of resistance was performed using a d.c. resistance module in PPMS (Quantum Design, Dynacool-9), by the standard four-electrode method in the constant current mode. The bulk samples for resistance measurements were made from LOPC powders, or graphite and rGO (The Sixth Element (Changzhou) Materials Technology) powders using cold isostatic pressing. Detailed procedures can be found in the Supplementary Information.

Simulations

The PES was searched by large-scale atomistic simulation with neural network potential (LASP)[41] software using the stochastic surface walking method[42]. To obtain a description of the PES near fcc C_{60} and to find the possible structures for LOPC, we performed a structural search and the work flow is described in Supplementary Information. To have a description of the PES in two dimensions, we used the Steinhardt-type OP, defined as

$$OP_l = \left(\frac{4\pi}{2l+1} \sum_{m=-l}^{l} |\overline{Y_{lm}(\mathbf{n})}|^2 \right)^{\frac{1}{2}},$$

to distinguish the geometrical features of the carbon isomers, where Y_{lm} is the spherical harmonic function of degree l and order m; $\mathbf{n}$ is the normalized direction between all bonded atoms and the bar over Y_{lm} means the average over all bonded atoms[43].

The charge differential density, electronic density of states, Raman, NMR and AIMD simulations were performed with the Vienna Ab initio Simulation Package (VASP)[44] software with the generalized gradient approximation[45] and with the Perdew–Burke–Ernzerhof[46] functional. The energy cutoff for the projector augmented-wave method (PAW)[47] basis set was 400 eV for AIMD and 500 eV for other DFT calculations. Gaussian-type smearing was used with an energy window of 0.1 eV. The self-consistent field convergence criteria were 0.1 meV for the AIMD simulations and 0.01 meV for the other DFT calculations. The Becke–Jonson damping DFT-D3 correction[48] was used. All calculations were done with the spin unrestricted except for the AIMD simulations. The transition state search calculations were done using transition state tools for VASP (VTST) with the nudged elastic band method[49]. The temperature (300 to 5,000 K) was controlled by rescaling the velocity every 5 fs, with SMASS = −1 and NBLOCK = 5 settings during AIMD simulations.

X-ray diffraction simulation was done using the REFLEX module in Materials Studio. The crystallite size, L_a, L_b or L_c, was considered in a range of 250 to 500 Å for broadening the peaks. The function was selected as pseudo-Voigt type. The pattern parameters are considered in the Rietveld refinement[50]. Raman spectra were calculated by a Raman off-resonance activity calculator in combination with VASP, which was developed by Alexandr Fonari (Georgia Tech) and Shannon Stauffer (UT Austin). NMR chemical shifts were simulated on the basis of the linear response method[51,52]. NEXAFS spectra were calculated by the equivalent core hole method[53], using our in-house code[54,55] interfaced with the Gaussian 09 package[56]. The electronic structure was computed at the DFT level with the hybrid B3LYP functional. Stick spectra were convoluted by a Gaussian function with a full-width at half-maximum of 0.4 eV for energies lower than 289.4 eV, 1.5 eV for energies above 291.4 eV and linearly increasing value from 0.4 to 1.5 eV for energies between 289.4 and 291.4 eV. Calibration was performed by aligning the simulated main π^* peak of C_{60} to the experimental value (284.5 eV) and the same shift was assumed for the other structures. More simulation details are included in the Supplementary Information.

Data availability

All data supporting the findings of this work are available within the paper and its Supplementary Information. Source data can be found at https://github.com/NiKun9/fullerene_evolution. Source data are provided with this paper.

Code availability

All density functional theory calculations were performed using VASP and Gaussian 09 software, which are commercially available at https://www.vasp.at/ and https://gaussian.com/. All structural search calculations based on neutral network potential were performed using LASP software, which is commercially available at http://www.lasphub.com and free for academic usage. The Raman off-resonance activity calculator is available at https://github.com/afonari/raman-sc.

39. Xu, J. et al. Multi-physics instrument: total scattering neutron time-of-flight diffractometer at China Spallation Neutron Source. *Nucl. Instrum. Methods Phys. Res. A* **1013**, 165642 (2021).
40. Arnold, O. et al. Mantid-data analysis and visualization package for neutron scattering and μ SR experiments. *Nucl. Instrum. Methods Phys. Res. A* **764**, 156–166 (2014).
41. Huang, S. D., Shang, C., Kang, P. L., Zhang, X. J. & Liu, Z. P. LASP: fast global potential energy surface exploration. *WIREs Comput. Mol. Sci.* **9**, e1415 (2019).
42. Zhang, X.-J., Shang, C. & Liu, Z.-P. From atoms to fullerene: stochastic surface walking solution for automated structure prediction of complex material. *J. Chem. Theory Comput.* **9**, 3252–3260 (2013).
43. Steinhardt, P. J., Nelson, D. R. & Ronchetti, M. Bond-orientational order in liquids and glasses. *Phys. Rev. B* **28**, 784–805 (1983).
44. Hafner, J. Ab-initio simulations of materials using VASP: density-functional theory and beyond. *J. Comput. Chem.* **29**, 2044–2078 (2008).
45. Perdew, J. P., Burke, K. & Ernzerhof, M. Generalized gradient approximation made simple. *Phys. Rev. Lett.* **77**, 3865–3868 (1996).
46. Ernzerhof, M. & Scuseria, G. E. ssessment of the Perdew–Burke–Ernzerhof exchange-correlation functional. *J. Chem. Phys.* **110**, 5029–5036 (1999).
47. Blöchl, P. E. Projector augmented-wave method. *Phys. Rev. B* **50**, 17953–17979 (1994).
48. Grimme, S., Antony, J., Ehrlich, S. & Krieg, H. A consistent and accurate ab initio parametrization of density functional dispersion correction (DFT-D) for the 94 elements H-Pu. *J. Chem. Phys.* **132**, 154104 (2010).
49. Sheppard, D., Xiao, P., Chemelewski, W., Johnson, D. D. & Henkelman, G. A generalized solid-state nudged elastic band method. *J. Chem. Phys.* **136**, 074103 (2012).
50. Young, R. A. *The Rietveld Method* Vol. 5 (International Union of Crystallography, 1993).
51. Yates, J. R., Pickard, C. J. & Mauri, F. Calculation of NMR chemical shifts for extended systems using ultrasoft pseudopotentials. *Phys. Rev. B* **76**, 024401 (2007).
52. Pickard, C. J. & Mauri, F. All-electron magnetic response with pseudopotentials: NMR chemical shifts. *Phys. Rev. B* **63**, 245101 (2001).
53. Plashkevych, O., Privalov, T., Ågren, H., Carravetta, V. & Ruud, K. On the validity of the equivalent cores approximation for computing X-ray photoemission and photoabsorption spectral bands. *Chem. Phys.* **260**, 11–28 (2000).
54. Li, X., Hua, W., Guo, J. & Luo, Y. Electronic structure of nitrogen-doped graphene in the ground and core-excited states from first-principles simulations. *J. Phys. Chem. C* **119**, 16660–16666 (2015).
55. Ma, Y. et al. Local structures of nitrogen-doped graphdiynes determined by computational X-ray spectroscopy. *Carbon* **149**, 672–678 (2019).
56. Frisch, M. et al. Gaussian 09, Revision D. 01 (Gaussian, 2009).

Additional information
Supplementary information The online version contains supplementary material available at https://doi.org/10.1038/s41586-022-05532-0.
Correspondence and requests for materials should be addressed to Rodney S. Ruoff or Yanwu Zhu.
Peer review information *Nature* thanks Yongjun Tian, Thomas Wågberg and the other, anonymous, reviewer(s) for their contribution to the peer review of this work. Peer reviewer reports are available.
Reprints and permissions information is available at http://www.nature.com/reprints.